buildings

MDPI

Article

Machine Learning-Based Methods for Predicting the Structural Damage and Failure Mode of RC Slabs Under Blast Loading

Jian Yang [1], Yan Hao [1], Dang Peng [2], Jun Shi [1,*] and Yi Zhang [3,*]

[1] School of Civil Engineering, Central South University, Changsha 410083, China; jianyangyy@126.com (J.Y.); 224812186@csu.edu.cn (Y.H.)
[2] Beijing Tianhe Qianyuan New Material Co., Ltd., Beijing 102299, China; samon_pd@163.com
[3] Academy of Combat Support, Rocket Force University of Engineering, Xi'an 710025, China
* Correspondence: csushijun@csu.edu.cn (J.S.); zhangyi_lijiacun@163.com (Y.Z.)

Abstract: Reinforced concrete (RC) slabs are the main load-bearing member of engineering structures, which may be threatened by blast loading. Predicting and analyzing the damage condition and failure mode of RC slab is a necessary means to ensure structural safety and reduce the potential hazards. In this study, two machine learning (ML) models are proposed using data from the published literature and complementary numerical simulations. By comparing six algorithms, it is determined that Extreme Gradient Boosting (XGBoost) is the optimal structural damage model and Categorical Boosting (CatBoost) is the optimal failure mode classification model. In addition, the Shapley additive explanations (SHAP) method was used to analyze the importance and correlation of features. The results show that the TNT charge mass, explosion distance, and compressive strength are the key features. On this basis, when the TNT charge mass is more than 2.5 kg, the sensitivity of the explosion distance increases, and when the compressive strength is more than 50 MPa, the impact on the structural damage is not significant. The research results can predict the structural damage and failure modes of RC slab under blast loading quickly and accurately, and provide guidance for the explosion-proof design of RC slabs.

Keywords: machine learning; blast loading; reinforced concrete slabs; damage prediction; Shapley additive explanation; failure mode

check for updates

Received: 21 March 2025
Revised: 5 April 2025
Accepted: 7 April 2025
Published: 8 April 2025

Citation: Yang, J.; Hao, Y.; Peng, D.; Shi, J.; Zhang, Y. Machine Learning-Based Methods for Predicting the Structural Damage and Failure Mode of RC Slabs Under Blast Loading. *Buildings* **2025**, *15*, 1221. https://doi.org/10.3390/buildings15081221

Copyright: © 2025 by the authors. Licensee MDPI, Basel, Switzerland. This article is an open access article distributed under the terms and conditions of the Creative Commons Attribution (CC BY) license (https://creativecommons.org/licenses/by/4.0/).

1. Introduction

Peace and development have become the themes of the day, but terrorism and accidental explosions still exist around the world. As a crucial component within the engineering structures, RC slabs are potentially vulnerable to the risks posed by terrorist assaults, industrial gas explosions, or various other hazards [1–4]. Under the action of blast loading, RC slabs are subjected to damage, and these effects not only severely damage the integrity of RC slabs, leading to the impairment of their use function, but also cause a significant reduction in their load-bearing capacity. Therefore, it is very important to study the damage condition and failure mode of RC slabs under blast loading. This can not only provide guidance for optimizing the blast-resistant design and construction of RC slabs, but also prevent the weak points of the components to effectively resolve the potential risks.

Traditionally, studies on the damage of RC slabs are mainly theoretical analyses [5,6], numerical simulations [1,7–11], and experiments [12–18]. However, they all have certain limitations. The theoretical analysis is influenced by the presuppositions, and the accuracy of the results needs to be verified. Numerical simulation is limited by modeling level and boundary conditions and cannot be predicted quickly. Explosion experiments are expensive

and risky, and cannot produce a lot of data, and it is difficult to conduct a significance analysis of the influence factors of RC slabs.

With the progress of society and the development of science and technology, more and more scholars have begun to apply new methods to scientific research. Machine Learning (ML), an essential division within Artificial Intelligence (AI), is a rapidly growing field of technology that furnishes techniques driven by data for extracting information from vast data sets [19–22]. In recent years, ML methods, as an effective data-driven strategy, have been widely used in the field of explosions. For example, Zhao et al. [23] trained several ML models on 260 sets of blast data to predict the displacement of RC slabs under blast loading, and validated the proposed method through three aspects: performance metrics, comparison with existing methods, and interpretability of the machine learning model, and the results showed that using the machine learning method is an accurate and fast way to predict the dynamic response of RC slabs under blast loading and they compared its performance with traditional methods. Li et al. [24] developed a Back Propagation Neural Network (BPNN) model, utilizing extensive numerical simulation data. This model was subsequently enhanced through a genetic algorithm approach, enabling swift predictions of the residual axial load capacity exhibited by RC columns subjected to blast loading. Neto et al. [25] used mixed experimental and numerical simulation data to train an Artificial Neural Network (ANN), and predicted efficiently the impulse generated by the explosion, the maximum displacement at the midpoint of the slab, and the residual strain, respectively. Dennis et al. [26] confirmed that Neural Networks (NNs) can be used to quickly predict the explosion impulse generated by explosions. The error of 81–87% of the prediction results is less than 10%, which indicates that the method is suitable and fast. Almustafa et al. [27] proposed a method based on the Random Forest (RF) algorithm for calculating the maximum displacement of RC slabs under blast loading. This method was trained using 150 samples from the published literature, and the results of the prediction show that the model is both accurate and efficient. Xu et al. [28] used the Beetle Antennae Search (BAS) method to improve BPNN to predict shock wave pressure of underground structure gas explosions. Hemmatian et al. [29] adopted the Bayesian Regularization Artificial Neural Network (BRANN) method. The impact wave energy and compressive peak value in swelling steam explosions of boiling liquid are accurately predicted. Pannell et al. [30] proposed a regression prediction model based on the Gaussian function, which used verified numerical models to build data sets, and this method can be used to quickly predict the near-field explosion impulse of various proportional detonation distances. Li et al. [31] predicted Boiling Liquid Expanding Vapor Explosions (BLEVEs) based on an ML algorithm and the Computational Fluid Dynamics (CFD) method. The results show that the optimal Transformer model can fully characterize the BLEVE load on the structure.

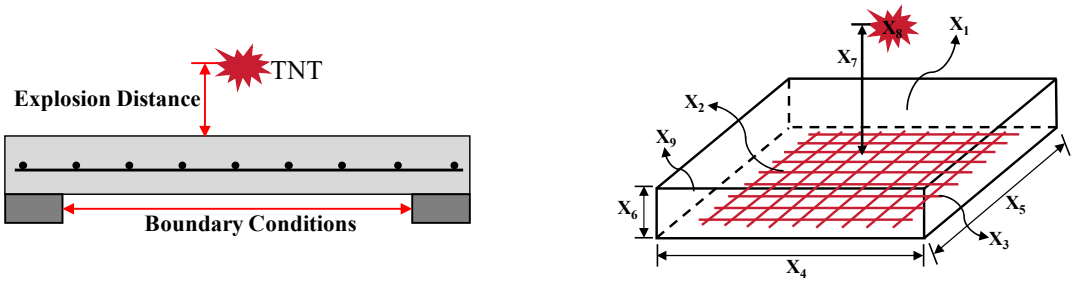
The above studies show that ML models have high accuracy, high efficiency, and high data processing capability, and have obvious advantages in application in the field of explosions. However, so far, in-depth studies on the structural damage and failure modes of RC slabs under blast loading have been very limited. A key challenge is the scarcity of real data used to train the model.

Therefore, this study presents for two ML models for predicting structural damage and failure modes of RC slabs. Six models were trained using 260 data collected from the literature and 300 numerical simulation data and the parameters used for both models were seven structural and two blast parameters. The first model was used to predict the explosion crater size of RC slabs and the importance ranking and dependency analysis of the features were performed using the SHAP algorithm. The second model was used to predict the failure mode of RC slabs under blast loading and is based on the evaluation metrics and a probabilistic confusion matrix.

2. Data Description

2.1. Literature Data and Feature Selection

The test setup for an RC slab exposed to explosive loading consists of a slab specimen, a support frame, and explosives. The slab specimen is placed on a support frame with the RC slab restrained on two sides and free on the other two sides, as shown in Figure 1a. During the explosion test, the explosive is usually suspended from the center of the RC slab. After the explosion, crater size and failure mode are two of the easy indexes to obtain in RC slab, and are often used as important parameters to evaluate the degree of explosion damage, since the range of feature representations often exerts a considerable influence on the predicted outcome in the application of ML models. Therefore, to comprehensively quantify the experimental process of the explosion, this paper uses nine features as its input. The selection of specific features is shown in Figure 1b.



(**a**) (**b**)

Figure 1. Arrangement and feature selection diagrams of RC slabs under blast loading: (**a**) explosive device diagram; (**b**) features selection.

In this study, the chosen input features are categorized into three distinct groups, taking into account their inherent characteristics. The primary group pertains primarily to concrete specimens, encompassing factors such as the compressive strength of concrete (X_1), the reinforcement ratio (X_2), the yield strength of steel (X_3), as well as the dimensional parameters associated with the specimens: the length of the slabs (X_4), the width of the slabs (X_5), and the thickness of the slabs (X_6). The second category of input features is primarily concerned with blast loading, which includes the explosive distance (X_7) and the TNT charge mass (X_8). The third category of input features is the boundary condition (X_9), which belongs to the classification feature, including being secured on all four edges (B_1), simply supported at all four edges (B_2), short edges secured and long edges unrestricted (B_3), short edges simply supported and long edges unrestricted (B_4), three edges secured and one edge unrestricted (B_5), long edges secured and short edges unrestricted (B_6), long edges simply supported and short edges unrestricted (B_7), square slabs with secured opposite edges and unrestricted opposite edges (B_8), and square slabs with simply supported opposite edges and unrestricted opposite edges (B_9).

To ensure the authenticity of the data, this paper collected experimental and numerical simulation data from 24 published studies [1,10,12,16,17,32–50] at home and abroad, among which there were some problems of incomplete data and missing feature data. In this paper, to better train the model, incomplete information is eliminated, leaving a total of 260 sets of data. Finally, the available data are sorted and converted into a database. The database source information is shown in Table 1 and the range of data is shown in Table 2.

Table 1. The database source information for data collected from the literature.

No.	Author	Number	Type	No.	Author	Number	Type
1	Zhao et al., 2013 [1]	10	E [a] + N [b]	13	Li et al., 2016 [39]	2	E [a]
2	Zhao et al., 2018 [10]	4	E [a] + N [b]	14	Liu et al., 2023 [40]	2	E [a]
3	Kumar et al., 2020 [12]	10	E [a] + N [b]	15	Wang Qiang., 2019 [41]	25	E [a] + N [b]
4	Wang et al., 2013 [16]	6	E [a] + N [b]	16	Ruggiero et al., 2019 [42]	3	E [a]
5	Wu et al., 2009 [17]	2	E [a]	17	Shi et al., 2015 [43]	4	E [a]
6	Cai et al., 2022 [32]	10	E [a]	18	Xu et al., 2020 [44]	20	E [a] + N [b]
7	Castedo et al., 2015 [33]	20	E [a] + N [b]	19	Wang et al., 2023 [45]	4	E [a]
8	He Fukang., 2018 [34]	34	N [b]	20	Wang et al., 2012 [46]	2	E [a]
9	Hou et al., 2016 [35]	12	N [b]	21	Wang Wei., 2012 [47]	12	N [b]
10	Hou et al., 2013 [36]	32	E [a] + N [b]	22	Xu Wenfeng., 2022 [48]	26	N [b]
11	Sun et al., 2019 [37]	10	N [b]	23	Yao et al., 2023 [49]	1	E [a]
12	Li et al., 2015 [38]	4	E [a] + N [b]	24	Zhao et al., 2021 [50]	5	E [a]

[a] Experiment, [b] Numerical simulation.

Table 2. Range of data in the open literature.

No.	Feature	Units	Experiment Range	Simulation Range
X_1	Compressive Strength	MPa	23.4~75	25~68
X_2	Reinforcement Ratio	%	0.15~1.73	0.15~1.70
X_3	Steel Yield Strength	MPa	235~630	235~500
X_4	Length	cm	50~400	50~400
X_5	Width	cm	40~400	40~400
X_6	Thickness	cm	3~50	3~50
X_7	Explosion Distance	m	0.1~2.1	0.1~2.1
X_8	TNT Charge Mass	kg	0.2~15	0.2~10
X_9	Boundary Condition	$B_1(46)$, $B_2(40)$, $B_3(36)$, $B_4(26)$, $B_5(25)$, $B_6(17)$, $B_7(17)$, $B_8(38)$, $B_9(15)$		

2.2. Numerical Simulation of Supplementary Data

ML models need a large amount of data as a support. Due to the limited amount of data in the literature, this paper needs to supplement some of the data, so this paper uses LS-DYNA R14 simulation software to simulate the RC slabs in reference [16], which is an example of structural damage simulation results of the RC slabs under explosion loading.

The dimensions of the RC slab in the literature [16] were 1100 mm × 1000 mm × 40 mm, with compressive and tensile strengths of 39.5 MPa and 4.2 MPa. The reinforcement arrangement was made with a single layer of bi-directional reinforcement with a diameter of 6 mm and a spacing of 75 mm, and with a yield strength of 600 MPa. The TNT charge mass were used and placed at the center of the slab at a height of 0.4 m. The experiment is shown in Figure 2. A finite element (FE) model was established, as shown in Figure 3. In order to improve the efficiency and consider the symmetry of the model, this paper adopts the FSI (Fluid–Structure Interaction) method to establish the 1/4 FE model, in which the mesh sizes of the concrete and the steel reinforcement are set to 5 mm, and the air to 10 mm. The concrete is modeled by the *MAT_RHT material model, and the steel reinforcement is modeled by the *MAT_PLASTIC KINEMATIC modeling. TNT charge mass and air are co-created with the *ALE_MULTI_MATERIAL_GROUP model for TNT explosive filling by the Initial Volume Fraction Method, while RC slabs and plywood are defined by the automatic surface-to-surface contact method. Since the explosion of the RC slab is in the air domain, the final interaction between the concrete and steel reinforcement and the RC slab and air domains is carried out via *CONSTRAINED_LAGRANGE_IN_SOLID.



Figure 2. Explosion test [16].

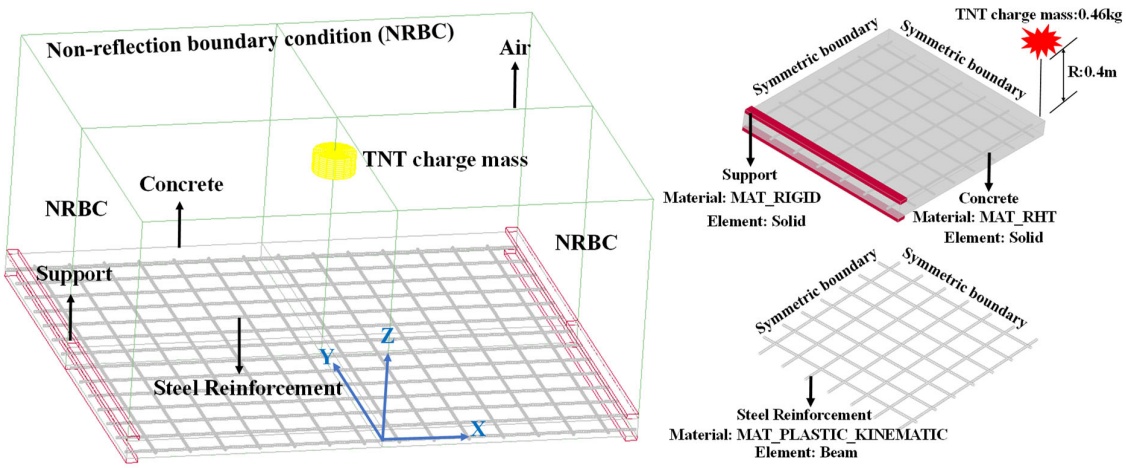


Figure 3. The establishment of FE model: (**a**) FE model; (**b**) RC slab and support.

The comparison of damage dimensions of RC slab under explosion load between test and numerical simulation is shown in Figure 4. The shock wave generated by the TNT explosion passes through the back of the RC slab and generates reflected stretch waves, which forms cracks on the back of the RC slab and causes the back of the RC slab to spall. Figure 4 shows the comparison of RC slab spalling pit sizes under three working conditions of 0.31 kg, 0.46 kg, and 0.55 kg. From Table 3, we can see that the numerical simulation data are 93 mm, 115 mm, and 156 mm, respectively, and the error between them and the experimental values of 90 mm, 120 mm, and 150 mm is −3.33%, 4.17%, and −4.00%, respectively, all of which are below 5%. In summary, the numerical simulation results based on the FE model are in good agreement with the experimental results, so the numerical simulation method adopted in this paper can be used to calculate the crater size of the structure.

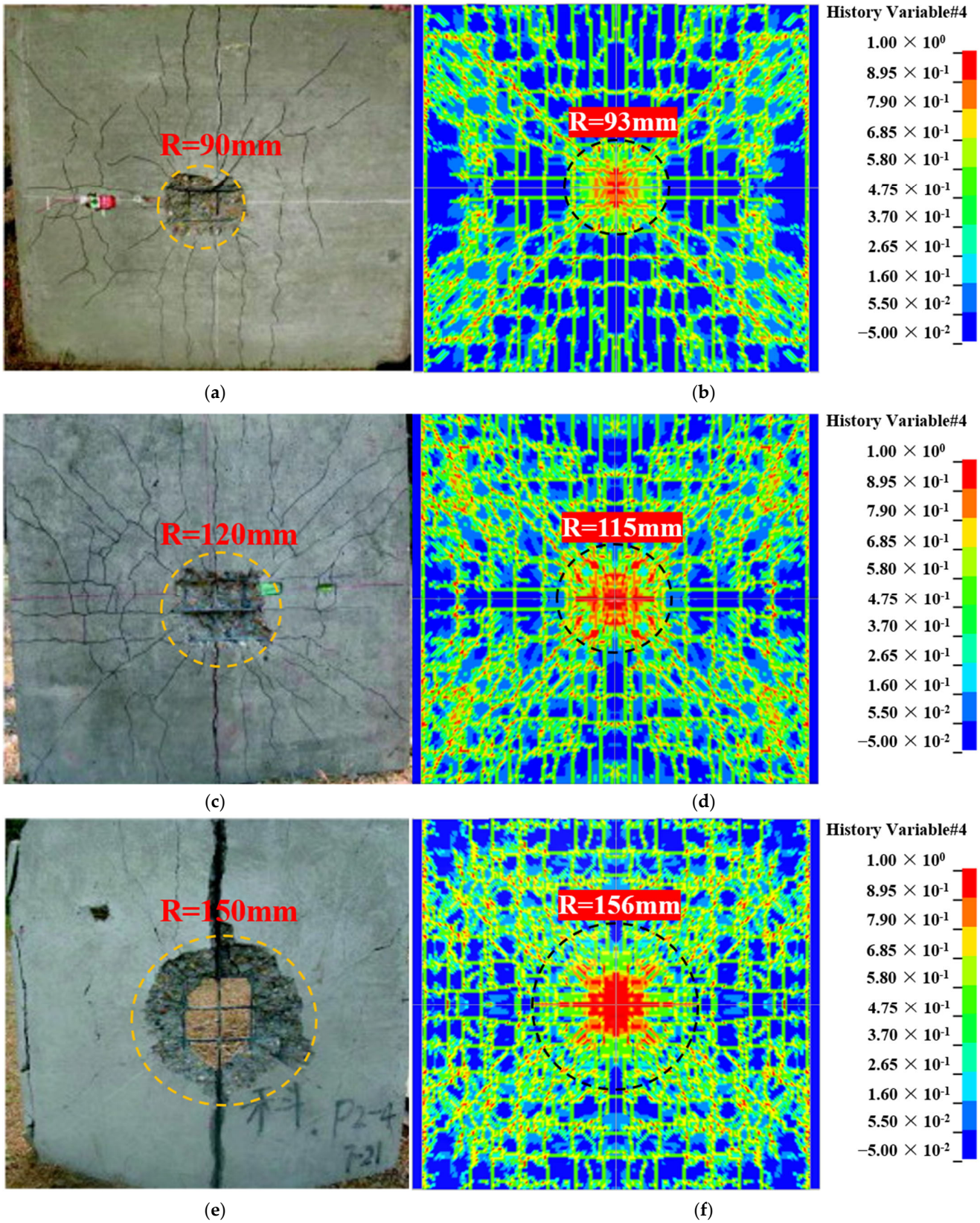


Figure 4. Experimental and simulation comparisons of crater size on the bottom face: (**a**) experimental (0.31 kg) results [16]; (**b**) numerical (0.31 kg) results; (**c**) experimental (0.46 kg) results [16]; (**d**) numerical (0.46 kg) results; (**e**) experimental (0.55 kg) results [16]; (**f**) numerical (0.55 kg) results.

Table 3. Error analysis of experimental data and numerical simulation data.

TNT Charge Mass (kg)	Explosion Distance (m)	Spall Radius (mm)		(Experiment-Numerical)/ Experiment
		Experiment Results	Numerical Results	
0.31	0.4	90	93	−3.33%
0.46	0.4	120	115	4.17%
0.55	0.4	150	156	−4.00%

In this paper, 300 sets of data (Table 4) were supplemented by applying the numerical simulation results, on the basis of which the three damage modes of bending failure (BF), bending shear failure (BSF), and shear failure (SF) of RC slabs were organized accordingly based on the database of this paper and with reference to the literature [51]. Finally, 300 data sets were combined with the literature data for a total of 560 data sets. On this basis, 560 sets of data were used for regression prediction of structural damage, while only 300 sets of data from the simulation could be utilized to classify and predict the failure modes of RC slabs due to the absence of the failure modes of slabs in the literature data.

Table 4. The value ranges of the numerical simulation data.

No.	Feature	Units	Simulation Range
X_1	Compressive Strength	MPa	25~70
X_2	Reinforcement Ratio	%	0.15~1.73
X_3	Steel Yield Strength	MPa	250~600
X_4	Length	cm	50~400
X_5	Width	cm	40~400
X_6	Thickness	cm	3~50
X7	Explosion Distance	m	0.1~2.1
X_8	TNT Charge Mass	kg	0.2~15
X_9	Boundary Condition	$B_1(30)$, $B_2(50)$, $B_3(65)$, $B_4(30)$, $B_5(10)$, $B_6(15)$, $B_7(25)$, $B_8(30)$, $B_9(45)$	

2.3. Data Preprocessing

Kernel Density Estimation (KDE) is a method used in probability theory to estimate unknown density functions. Through the KDE diagram (Figure 5), it can be intuitively seen that the distribution characteristics of the data samples and the distribution of the training set and the test set are basically consistent, so that we can test the consistency of the data set. Meanwhile, the detailed statistics of the data set are shown in Table 5.

Table 5. Statistical description of features.

Variance	Feature/Output	Units	Ave [a]	Std [b]	Max	Min
X_1	Compressive Strength	MPa	42.67	11.56	75.00	23.4
X_2	Reinforcement Ratio	%	0.91	0.39	1.73	0.15
X_3	Steel Yield Strength	MPa	457.09	94.04	630.00	235.00
X_4	Length	cm	186.81	97.75	400.00	50.00
X_5	Width	cm	173.60	102.88	400.00	40.00
X_6	Thickness	cm	18.46	13.83	50.00	3.00
X_7	Explosion Distance	m	0.27	0.35	2.10	0.10
X_8	TNT Charge Mass	kg	2.32	3.06	15.00	0.20
X_9	Boundary Condition	$B_1(76)$, $B_2(90)$, $B_3(101)$, $B_4(56)$, $B_5(35)$, $B_6(32)$, $B_7(42)$, $B_8(68)$, $B_9(60)$				
Y	Explosion Crater Size	cm	43.20	33.78	165.00	0.00

[a] Average. [b] Standard deviation.

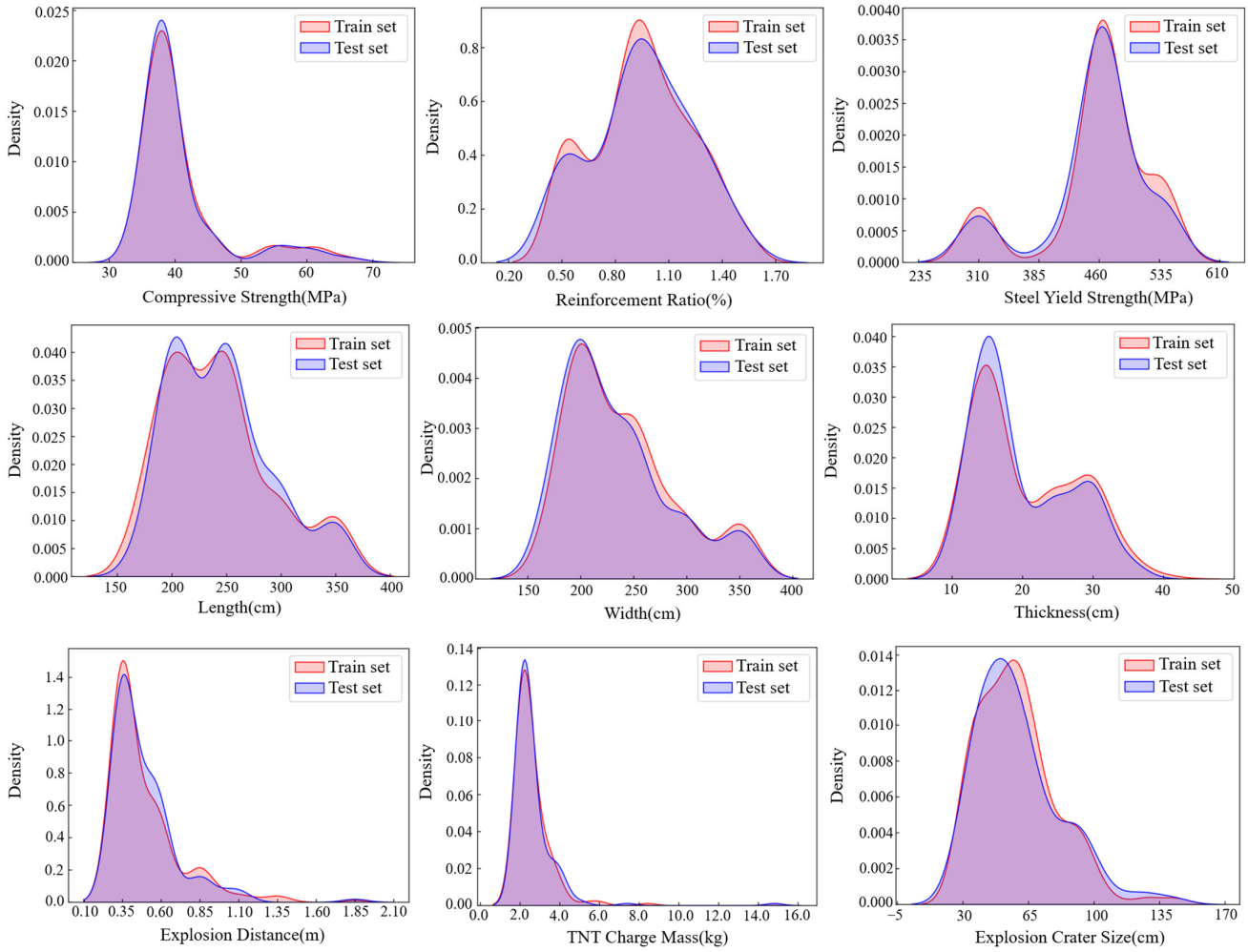


Figure 5. KDE distribution of input and output parameters.

Since ML models cannot effectively recognize and utilize classification features, we need to convert the boundary conditions into numerical form so that the model can be used for subsequent training and prediction. For this purpose, this paper uses One-Hot Encoding to convert discrete classification features into binary vectors. However, the One-Hot Encoding vector has some shortcomings, such as high dimension, sparse dispersion, and lack of semantic relationships between different features. To solve these problems and make the structure of the data more reasonable, this paper introduces an embedding layer based on an NN and uses the embedding layer to embed the discrete sparse binary vectors, to map them to the continuous and tight word embedding space. The core idea is that the embedding layer maps sparse binary vectors into a low-dimensional, continuous vector space, effectively compressing the representations while preserving the semantic relationships between features. Through training, the embedding layer learns to locate similar categories closer together in the vector space by optimizing a distance metric. This approach allows the model to infer potential relationships between categorized features, thereby improving computational efficiency and prediction accuracy. This approach, inspired by semantic embedding techniques in NLP [52,53], enables the model to learn potential relationships between features, thereby improving efficiency and interpretability. A diagram of the embedding layer mapping is shown in Figure 6.

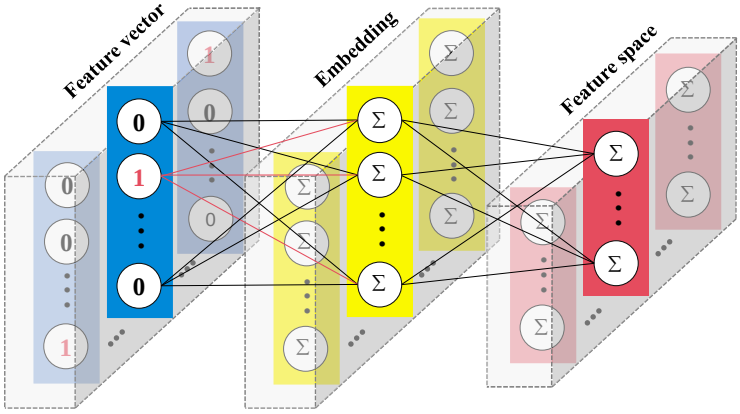


Figure 6. Numerical transformation of boundary conditions.

In the data preprocessing stage, normalization is an important part of optimizing model performance. Since there may be significant magnitude differences between different features in the raw data, such un-normalized data can directly affect the training efficiency of the model. Taking Support Vector Machine (SVM) and Back Propagation Neural Network (BPNN) as examples, these algorithms are more sensitive to feature scales. To address this issue, this study introduces the min-max normalization method, which compresses each feature value into a normalized interval of [0,1] through a linear transformation with the mathematical expression given in Equation (1).

$$x_{new} = \frac{x - x_{\min}}{x_{\max} - x_{\min}} \tag{1}$$

where $x_{\max}$ and $x_{\min}$ are the maximum and minimum values of the feature x, respectively.

2.4. Feature Engineering

After preprocessing the data, this paper needs to study the correlation between features, as it can help us understand the interactions between features and remove redundant or highly correlated features to avoid problems such as multicollinearity and overfitting of the model. Since the data distribution in this study does not conform to the normal distribution in the strict sense, the Spearman correlation coefficient is adopted in this paper; that is, the rank of two variables is used to measure their correlation, and the calculation is shown in Equation (2).

$$r_s = 1 - \frac{6\sum_{i=1}^{n} d_i^2}{n(n^2-1)} \tag{2}$$

where r_s represents the Spearman correlation coefficient, d_i represents the difference in rank of each pair of observations (x, y), and n represents the number of observed objects. After the above calculation, the results were expressed in the form of a matrix, and the corresponding Spearman heat map was constructed for visual analysis, as shown in Figure 7. It can be seen that the correlation coefficient between the length and the width of the slab reaches 0.84, showing a strong correlation, while the other features show a weak correlation and moderate correlation. Strong correlation may lead to multicollinear problems in the model, but further analysis shows that the two directions of RC slabs are affected by the size setting, and the strong correlation does not represent the inherent causality. Therefore, this article chooses to preserve both features. That is, all features can be trained for subsequent models.

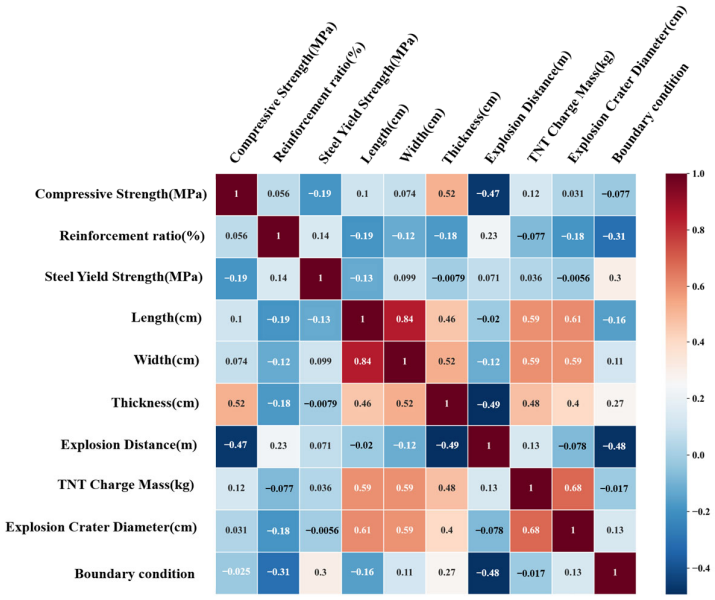


Figure 7. Spearman correlation coefficient matrix of input and output parameters.

3. Methodology

Figure 8 shows the method flow used in this study. First, four suitable ensemble models and two ML models are constructed for the characteristics of a small sample data set, which are that it is easy to overfit, difficult to converge, and exhibits low training efficiency: (1) Extreme Gradient Boosting (XGBoost), (2) Back Propagation Neural Network (BPNN), (3) Support Vector Machine (SVM), (4) Random Forest (RF), (5) Light Gradient Boosting Machine (LightGBM), and (6) Categorical Boosting (CatBoost). The principles of these six ML algorithms are shown in Figure 9. The input features and the data used have been mentioned in Section 2. All models are implemented using the scikit-learn library [54] within the Python 3.9 environment. Then, the data set is randomly divided, 80% of which is the training set and 20% is the test set. The training set is then used for model training, and the test set is used to evaluate the model, and finally the optimal model for predicting structural damage and failure mode is selected.

3.1. Machine Learning Methods

3.1.1. Extreme Gradient Boosting (XGBoost)

Extreme Gradient Boosting (XGBoost) is an efficient, flexible, and highly accurate algorithm for extreme gradient lifting proposed by Chen and Guestrin [55] in 2016, building upon the Gradient Boosting Decision Trees (GBDT) framework [56]. GBDT, introduced by Friedman (2001) [56], is an ensemble learning method that iteratively combines weak learners (typically decision trees) to minimize a differentiable loss function via gradient descent. Unlike traditional GBDT, XGBoost acts as a forward addition model; the fundamental principle of the algorithm involves amalgamating multiple weak learners to form a robust learner, as shown in Figure 9a. That is, the gradient enhancement is used to realize the integrated learning of multiple CART (Classification and Regression Trees) submodules [57,58]. Then, the loss function undergoes a second-order Taylor expansion, and regular terms are explicitly added to control the complexity of the model, reduce the variance of the model, effectively prevent the overfitting of the model, and improve the generalization ability of the model, to achieve the purpose of engineering application.

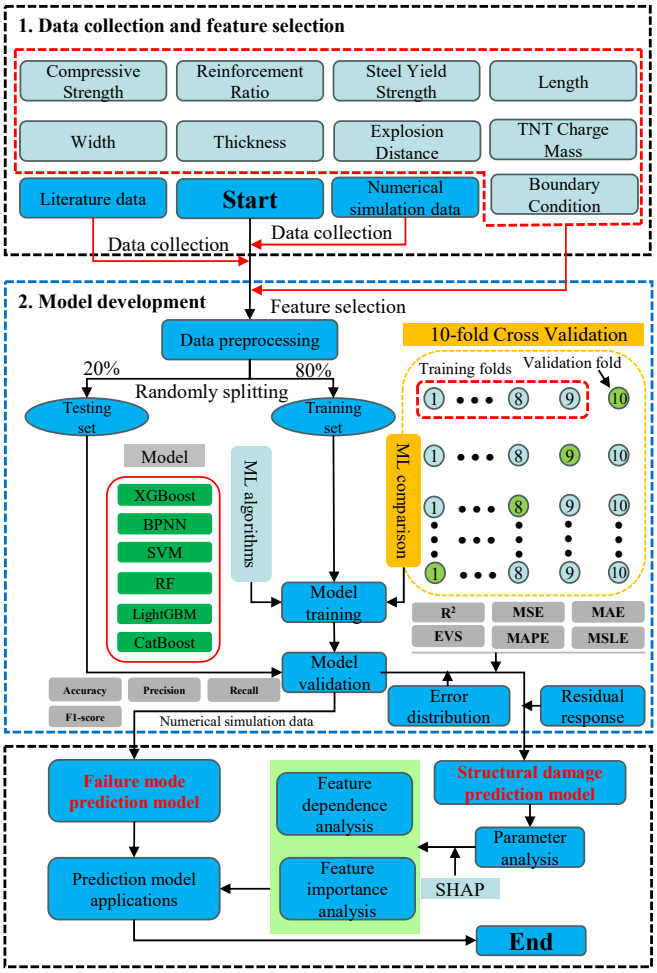


Figure 8. Flowchart of the study.

3.1.2. Back Propagation Neural Network (BPNN)

The Back Propagation Neural Network (BPNN) is a multi-layer feedforward network trained using the error inverse propagation algorithm, which is composed of forward computation conduction and error inverse conduction, and has a good ability to process nonlinear information. A BPNN is composed of several neuronal nodes, which are usually divided into an input layer, hidden layer, and output layer [59], as shown in Figure 9b. In general, NNs with multiple hidden layers generally excel in generalization and prediction accuracy but require longer training times. For the purpose of general mappings, a single-hidden-layer neural network (NN) structure has been shown to achieve satisfactory prediction accuracy [60]. Therefore, this study opts for the single-hidden-layer NN structure. The chosen iteration count is 1000, with a learning rate set at 0.05, while all other parameters are maintained at their default settings. The input layer of the backpropagation neural network (BPNN) model comprises nine input nodes, reflecting the nine input features required for predicting the diameter of the explosion crater. The output layer consists of a single node, representing the predictor variable. The data flows through the entire network from the input layer, with the input signal being processed layer by layer, ultimately reaching the output layer. Subsequently, the error between the output and the actual expectation is propagated backward layer by layer, with continuous updating and optimization of the weights of each neuron to decrease the error. Finally, after repeated learning and training, the obtained results are converted into outputs through activation functions.

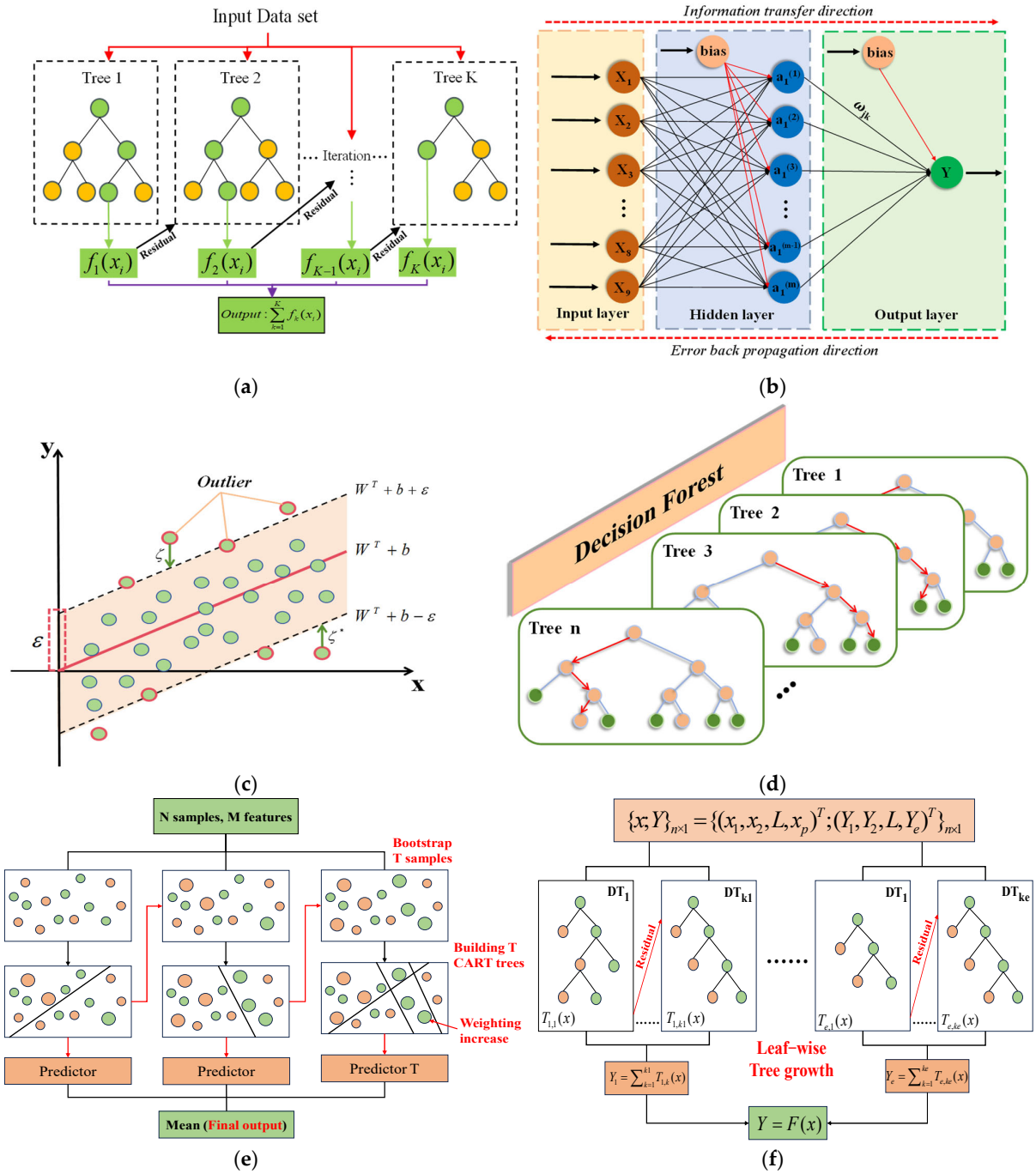


Figure 9. Schematic diagrams of six ML algorithms used in this study: (**a**) XGBoost; (**b**) BPNN; (**c**) SVM; (**d**) RF; (**e**) LightGBM; (**f**) CatBoost.

3.1.3. Support Vector Machine (SVM)

Support Vector Machine (SVM) is an ML model initially introduced by the Soviet mathematician Vapnik [61] in 1995, which is based on the VC (Vapnik-Chervonenkis) dimension theory and the basic principle of structural risk minimization. It is divided into classification models Support Vector Classification (SVC) and regression models Support Vector Regression (SVR). Unlike typical prediction problems, the SVM model permits a degree of tolerance. The loss is computed solely when the disparity between $f(x)$ and y surpasses the predefined tolerance, which is equivalent to setting up an isolation zone with a distance of ε on both sides of the linear function $f(x)$, as shown in Figure 9c. However, when solving practical problems, the SVM model exhibits a heightened sensitivity towards

abnormal data and is susceptible to overfitting, so relaxation variables ξ and ξ^* are added; that is, some samples can be excluded from the interval band and recorded as losses, thus improving the generalization ability of the model.

3.1.4. Random Forest (RF)

Random Forest (RF) is an integrated classifier that is trained by multiple decision trees [62]. RF uses the statistical technique Bootstrap to randomly and iteratively extract samples from the initial training data set, create a new set of training samples, and construct decision trees to form a random forest. During the model construction and training process, the feature selection of each decision tree node is randomized. Each decision tree assigns samples to different branches according to the selected feature attributes, thus building the node and branch structure of the decision tree, and then recursively until all nodes are divided and the stopping condition is reached. Finally, the prediction results of multiple decision trees are integrated, and the final prediction value is derived by averaging the results of multiple decision trees. The diagram is shown in Figure 9d.

3.1.5. Light Gradient Boosting Machine (LightGBM)

Light Gradient Boosting Machine (LightGBM) is a decision tree-based gradient boosting machine learning algorithm, widely used in classification and regression problems. Compared with the traditional Gradient Boosting Decision Tree (GBDT), LightGBM adopts the histogram algorithm in finding split points, and adds gradient one-sided sampling and independent feature merging [63]. Gradient one-sided sampling enables the LightGBM algorithm not only to maintain the accuracy of information gain evaluation, but also to have more accurate sampling results and higher learning speed at the same sampling rate. Independent feature merging reduces the feature dimensions through feature bundling and further improves the algorithm efficiency. The diagram is shown in Figure 9e.

3.1.6. Categorical Boosting (CatBoost)

The Categorical Boosting (CatBoost) algorithm [64] is a gradient boosting ML library open-sourced by Yandex in 2017, which uses preprocessing to deal with categorization features in the training process, and utilizes the sort boosting strategy to solve the gradient bias and prediction bias problems in the gradient boosting algorithm, while choosing the symmetric decision tree structure as the basic structure of the algorithm to calculate and control the number of leaf nodes, in order to improve the prediction speed of the constructed model and to avoid overfitting. The diagram is shown in Figure 9f.

3.2. Cross Validation

In this paper, the 10-fold Cross-Validation (10-CV) method is chosen to reduce the risk of overfitting, and the parameters of the ML models are adjusted and evaluated. The core idea is to divide 80% of the training set into 10 equal parts, rotate nine of them for training and the remaining one for validation, and separate 20% of the test set from them. Finally, the average value of the 10 results is used as the final performance evaluation of the model (Figure 10).

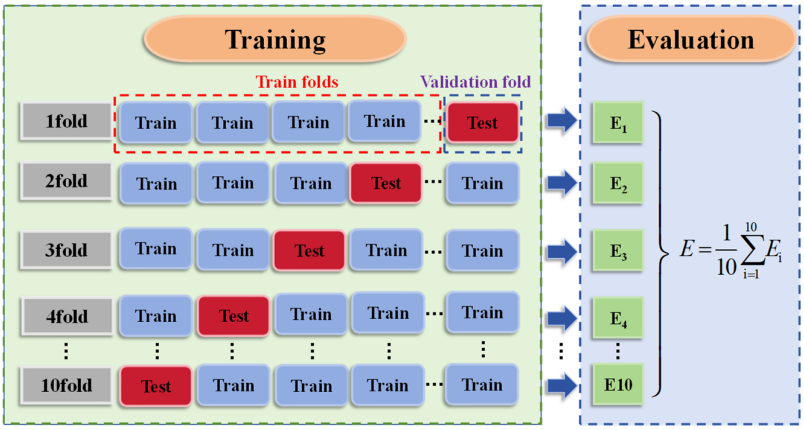


Figure 10. Flowchart of 10-fold cross-validation.

4. Structural Damage Prediction Models

In this section, six structural damage prediction models were trained using 560 sets of data and compared in terms of metrics evaluation, data point distribution, and residual response to obtain the ML model with the best prediction performance, on the basis of which the importance ranking and correlation analysis of the feature parameters were performed based on the Shapley additive explanations (SHAP) algorithm.

4.1. Hyperparameter Optimization

Before choosing a suitable ML model for data training, different combinations of hyperparameters in the model can lead to completely different model behaviors and performances. Thus, optimizing the hyperparameters of the ML algorithm is imperative for achieving enhanced prediction accuracy, quicker convergence, mitigated overfitting, and increased model stability. This study adopted the 10-CV and Bayesian Optimization (BO) methods to adjust the hyperparameters of the six ML models.

In the process of hyperparameter optimization, BO performs a 10-CV evaluation of the current hyperparameter configuration, and the results are used to continuously update the probabilistic proxy model based on Gaussian processes, thus updating the posterior probability of the optimization function, and then the acquisition function selects the next evaluated hyperparameter configuration according to the current posterior probability. After several rounds of iteration, the optimal hyperparameter combination is finally obtained. Based on ref. [65], this paper determined the optimized hyperparameters of six algorithms and their range, as shown in Table 6. For hyperparameters that are not displayed, the default values are used.

Table 6. Hyperparameter tuning of the six ML models.

Algorithms	Hyperparameters	Range	Optimized Value
XGBoost	n_estimators	[100, 500]	400
	learning_rate	[0.01, 0.2]	0.1
	min_child_weight	[1, 5]	4
	max_depth	[1, 20]	5
BPNN	hidden_layer_sizes	[(10,)~(200,)]	(26,)
SVR	C	[1, 1500]	1000
	gamma	[0.001, 1]	0.04
	kernel	[‘linear’, ‘rbf’, ‘poly’]	rbf

Table 6. *Cont.*

Algorithms	Hyperparameters	Range	Optimized Value
RF	n_estimators	[100, 500]	500
	min_samples_split	[1, 8]	5
	min_samples_leaf	[1, 4]	2
LightGBM	n_estimators	[100, 500]	400
	learning_rate	[0.01, 0.6]	0.3
	num_leaves	[30, 120]	50
	min_child_samples	[10, 40]	30
CatBoost	l2_leaf_reg	[1, 10]	6
	learning_rate	[0.01, 0.2]	0.2
	depth	[2, 10]	5

4.2. Evaluation Indicators

To assess the precision of the explosion crater size prediction model and analyze its capability in forecasting, six indexes including Mean Absolute Error (MAE), Mean Square Error (MSE), coefficient of determination (R^2), Explained Variance Score (EVS), Mean Absolute Percentage Error (MAPE), and Mean Squared Logarithmic Error (MSLE) are used in this paper to evaluate the explosion crater size prediction model, which are shown in Equations (3)–(8).

$$R^2 = 1 - \frac{\sum_i (y_i - \hat{y}_i)^2}{\sum_i (y_i - \overline{y})^2} \tag{3}$$

$$MAE = \frac{1}{n}\sum_{i=1}^{n} |\hat{y}_i - y_i| \tag{4}$$

$$MSE = \frac{1}{n}\sum_{i=1}^{n} (\hat{y}_i - y_i)^2 \tag{5}$$

$$EVS = 1 - \frac{Var(y - \hat{y})}{Var(y)} \tag{6}$$

$$MAPE = \frac{100}{N}\sum_{i=1}^{N} \left|\frac{y_i - \hat{y}_i}{y_i}\right| \tag{7}$$

$$MSLE = \frac{1}{N}\sum_{i=1}^{N} (\ln(y_i + 1) - \ln(\hat{y}_i + 1))^2 \tag{8}$$

where $\hat{y}_i$ is the predicted value, y_i is the actual value, N is the total number of samples, $\overline{y}$ is the mean value of the samples, and Var is the variance. In this paper, these six evaluation metrics are used to analyze and compare the selected ML models from various aspects.

4.3. Comparison of Prediction Results for Different Models

To build a highly accurate and reliable regression prediction model, the ML model needs to be carefully selected to lay the foundation for subsequent parameter analysis. In this study, based on the literature [66,67], the predictive ability of six ML models is analyzed in detail by comparing them from three different perspectives: performance index evaluation, data point distribution, and model response residual.

In order to prevent the risk of overfitting, this paper adopts the 10-CV method to verify the evaluation indicators of the six models on the training set for 10 times (Table 7). The average (Ave) of the evaluation index represents the average performance of the predictive capacity, and the standard deviation (Std) indicates the stability of the model. The XGBoost model has the best predictive performance among the six models, with an

Ave error index of 0.688 for MSE, 0.386 for MAE, 3.645 for MAPE, and 0.022 for MSLE. The Ave model fit index, R^2, is 0.972 and EVS is 0.977. The CatBoost and BPNN models follow closely, while the SVR model has the worst prediction performance in comparison. In addition, comparing the Std of each evaluation index shows that the XGBoost model has high stability performance, while the SVR model has the worst stability. Therefore, based on the above comparisons, it can be concluded that the XGBoost model has the best prediction performance, while the SVR model has the weakest prediction ability.

Table 7. Evaluation of ML model indicators.

Model		R^2	MSE	MAE	EVS	MAPE	MSLE
XGBoost	Ave	0.972	0.688	0.386	0.977	3.645	0.022
	Std	0.011	0.117	0.029	0.008	0.416	0.026
BPNN	Ave	0.965	1.068	0.481	0.967	3.612	0.039
	Std	0.013	0.121	0.033	0.018	0.452	0.026
SVR	Ave	0.931	1.365	0.825	0.915	5.383	0.076
	Std	0.015	0.126	0.049	0.031	0.558	0.066
RF	Ave	0.961	0.790	0.440	0.968	3.942	0.042
	Std	0.013	0.120	0.032	0.023	0.503	0.030
LightGBM	Ave	0.954	0.836	0.435	0.967	4.101	0.040
	Std	0.017	0.130	0.031	0.021	0.495	0.031
CatBoost	Ave	0.970	0.651	0.398	0.974	3.885	0.035
	Std	0.011	0.122	0.025	0.019	0.451	0.028

After selecting the optimal model according to the index results of the validation set, this paper selects MSE as the loss function, and carries out 400 iterations according to the value of n_estimators after parameter optimization to draw the loss function curve (Figure 11). It can be seen from the curve that the performance of the XGBoost model on the training set and the validation set is very close, and the validation set does not fluctuate significantly, so it can be concluded that the model does not overfit. For the generalization ability of an ML model, its ability on unknown data needs to be verified. Therefore, the actual performance of the model on the test set is shown in Table 8, which shows that XGBoost also has strong generalization capabilities.

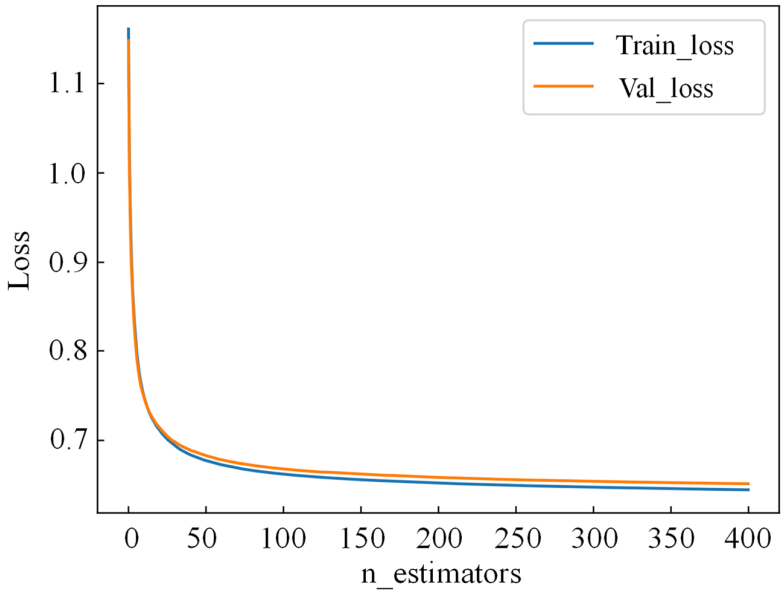


Figure 11. Performance of the XGBoost model trained with 10-CV.

Table 8. Performance evaluation on test sets.

Model	R^2	MSE	MAE	EVS	MAPE	MSLE
XGBoost	**0.979**	**0.675**	**0.379**	**0.981**	**3.639**	**0.020**
BPNN	0.968	1.043	0.468	0.970	3.608	0.035
SVR	0.935	1.335	0.816	0.920	5.376	0.071
RF	0.965	0.779	0.430	0.971	3.938	0.038
LightGBM	0.958	0.828	0.431	0.969	4.095	0.036
CatBoost	0.972	0.649	0.385	0.975	3.878	0.029

Bold values indicate the actual performance of the optimal model on the test set.

Figure 12 shows the distribution of predicted and actual data values for the training and test sets. The black line in the center represents the regression line. In the best case, if every point is on the regression line, the predicted values will be exactly the same as the actual values. In Figure 12a, the XGBoost model has the smallest bias with 448 data points in its training set. Within the error bounds of ±40% and ±20%, there are 418 data points and 383 data points, which account for 93.4% and 85.5% of the total number of training set data points, respectively. There are 112 data points in the test set, with 100 data points and 84 data points within the error bounds of ±40% and ±20%, accounting for 89.5% and 75.4% of the total test set, respectively. The number and percentage of deviations of the other models are shown in Table 9. The comparative analysis shows that the XGBoost model has better prediction results.

Table 9. Distribution of data points within the margin of error.

ML Model	Error Range	Train Points	Train Percentage	Test Points	Test Percentage
XGBoost	−20%~20%	383	85.5%	84	75.4%
	−40%~40%	418	93.4%	100	89.5%
BPNN	−20%~20%	381	85.1%	77	68.4%
	−40%~40%	405	90.4%	94	84.2%
SVR	−20%~20%	316	70.6%	67	60.1%
	−40%~40%	375	83.8%	83	73.7%
RF	−20%~20%	370	82.5%	71	63.2%
	−40%~40%	395	88.2%	88	78.9%
LightGBM	−20%~20%	364	81.3%	69	61.3%
	−40%~40%	392	87.5%	85	75.8%
CatBoost	−20%~20%	377	84.1%	82	73.5%
	−40%~40%	410	91.5%	97	86.3%

Figure 13 depicts a comparison between the actual and predicted responses for both the training and test data sets. At the top, the trend of actual and predicted values is depicted, while at the bottom, the residual values for the corresponding data points are displayed, and a residual range of ±10 cm is also marked at the zero baseline, where the closer the residual dispersion is to the zero baseline, the better the model predicts.

The XGBoost model shows relatively stable residual fluctuations in both the training and test sets, with residual values largely within 10 cm. The CatBoost and BPNN models follow closely behind, in contrast to the SVR model, which has the highest residual values, with a significant outlier in the predicted data points in the training set, where the actual value is 165 cm but the predicted value is 142 cm, resulting in a residual value of 23 cm. Similarly, there is a clear outlier in the test set. Clearly, the performance of the model on specific data in the training set affects its predictive performance on some of the data in the test set, resulting in the worst overall performance of the model. Finally, through the above analysis, we conclude that the XGBoost model has smaller residual errors and better

prediction results on both the training and test sets, and its performance is better than other methods. Based on the above three aspects of performance index evaluation, data point distribution, and model response residuals, this paper concludes that the optimal ML model is XGBoost. By accurately predicting the crater size, the optimal model can detect the potential structural damage as early as possible, so that targeted reinforcement measures can be taken to avoid more serious damage or collapse of the structure in subsequent use, which is of great significance for preventing the safety risks of the structure.

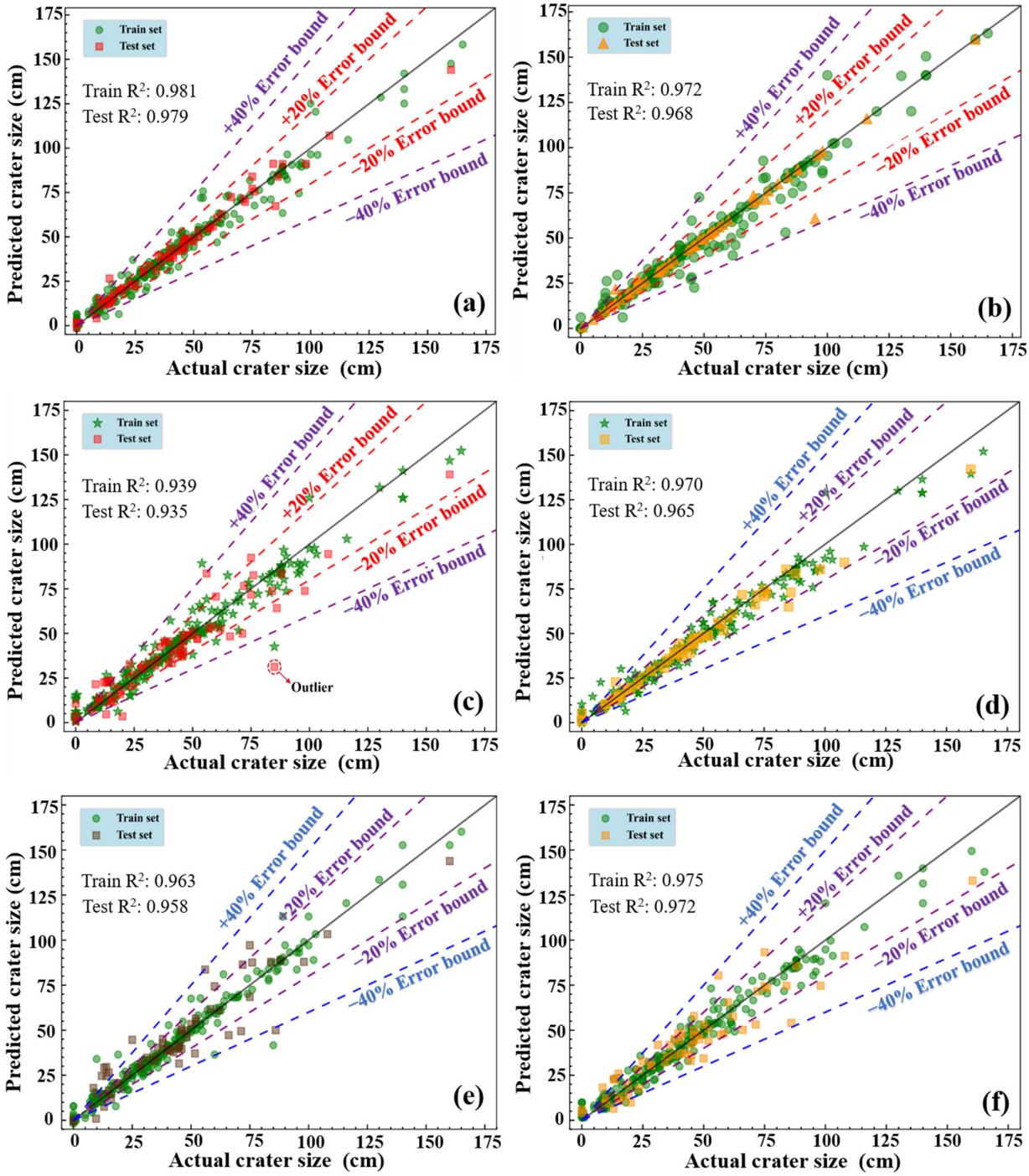


Figure 12. Margin of error between actual and predicted values: (**a**) XGBoost; (**b**) BPNN; (**c**) SVR; (**d**) RF; (**e**) LightGBM; (**f**) CatBoost.

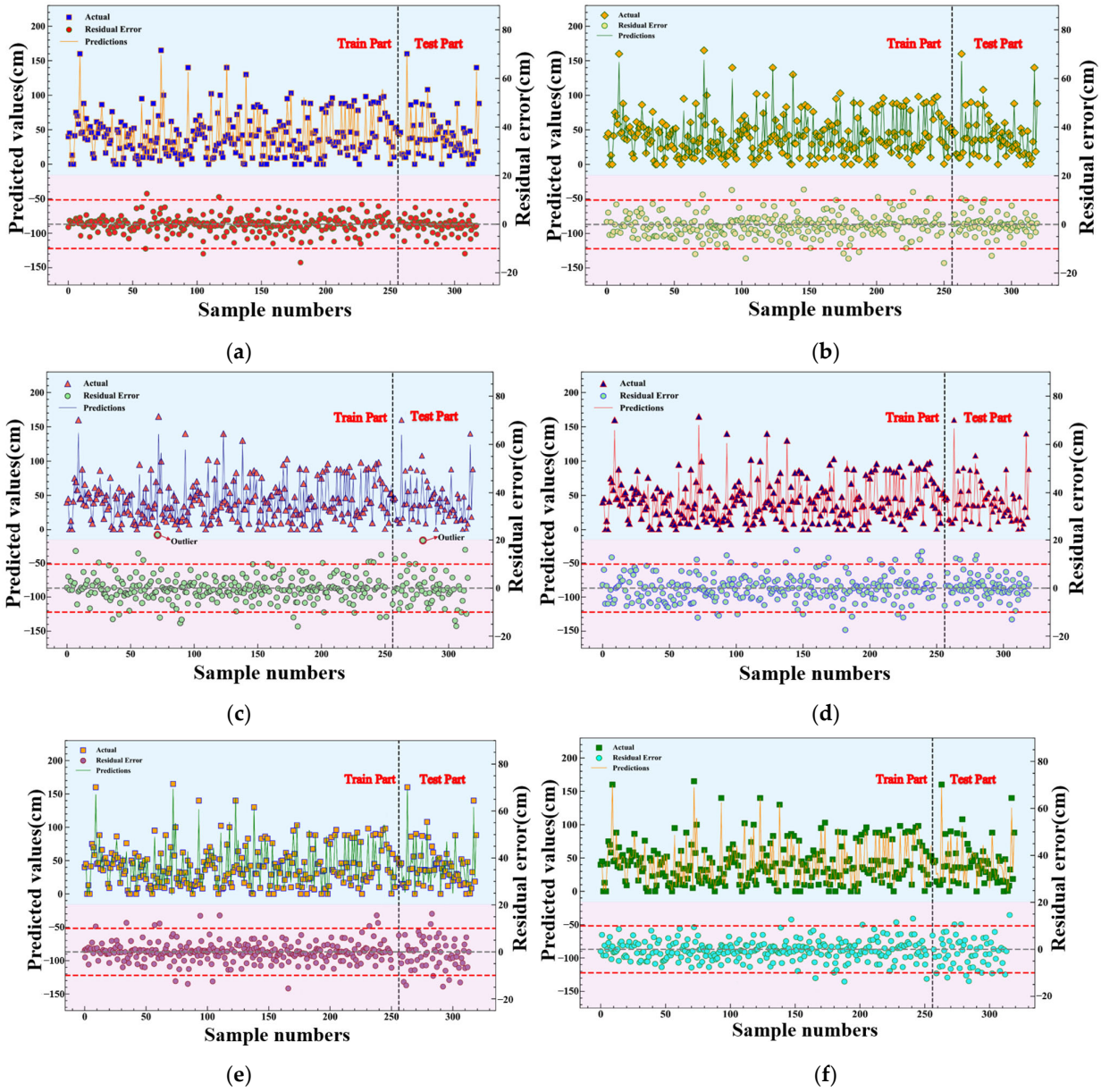


Figure 13. Residual plots of actual and predicted values: (**a**) XGBoost; (**b**) BPNN; (**c**) SVR; (**d**) RF; (**e**) LightGBM; (**f**) CatBoost.

In order to provide a more comprehensive assessment and a more recognized evaluation of the selected optimal ML model, the XGBoost model is now compared and analyzed with the existing methods (Table 10). By observing the errors of the burst crater dimensions in Table 10, it can be found that the prediction errors of the ML model are mostly lower than those of the numerical simulation methods, i.e., the prediction accuracy of the ML model is better than that of the numerical simulation methods. In summary, compared with the existing numerical simulation methods, the ML model has a better prediction effect, which indicates that it is an effective method to predict the diameter of the blast crater under the effect of explosive load.

Table 10. Comparison of ML method with existing methods.

No.	Source	Method	Experimental (mm)	Existing (mm)	Error	XGBoost (mm)	Error
1	Reifarth [68]	CONWEP	818	834	−1.96%	839	−2.57%
2			818	868	−6.11%	839	−2.57%
3	Zhao [10]	SPH	526	586	−11.41%	541	−2.85%
4			390	420	−7.69%	405	−3.85%
5	Hou [35]	ALE	46	38	17.39%	44	4.35%
6			52	44	15.38%	54	−3.85%
7			54	56	3.70%	55	−1.85%
8			95	74	22.11%	91	4.21%
9			98	84	14.29%	95	3.06%

4.4. Interpretive Analysis Using SHAP

Poor interpretability is an important factor hindering the application of ML algorithms in practical engineering [69]. Understanding why the model can predict the target variable according to the eigenvalue not only affects people's intuitive understanding of the prediction process, but also the reliability of the prediction results of the ML model, so it is necessary to analyze the interpretability of the prediction results. Lundberg et al. [70] proposed a unified interpretable ML method called Shapley additive explanations (SHAP). SHAP builds an additive interpretation model, and all features are treated as contributors; the sum of their contribution values is the final prediction of the model. The equation for calculating the contribution value is shown in Equation (9).

$$f(x) = g(z^*) = \varphi_0 + \sum_{i=1}^{M} \varphi_i z_i^* \tag{9}$$

where $f(x)$ is an ML model, which in this study is the XGBoost model. When a feature is observed, $z^* = 1$, otherwise 0; if i participates in the prediction process, M is the number of features, and ϕ_i is the contribution of the feature.

Figure 14a shows the mean SHAP value of the nine input features. According to the importance of the input features on the left side of the figure, it can be concluded that the three key factors affecting the size of the RC slab crater are TNT charge mass, explosion distance, and compressive strength. Among them, the TNT charge mass has an extremely important impact on the structural damage of the RC slab, while the impact of the other six input features on the RC slab crater size is relatively small, and the boundary conditions of the predicted results have the least impact. The above phenomenon indicates that the propagation trajectory of the blast wave will change due to the influence of the boundary conditions, but these changes have a limited effect on the dimensions of the crater, because they mainly affect the spatial distribution and propagation range of the blast wave energy, and do not directly affect the damage process of the RC slab. In contrast, the energy of the explosive and the physical properties of the target itself more directly determine the explosion crater size caused by the explosion.

Figure 14b illustrates the distribution of SHAP values for each input feature. Positive values on the horizontal axis indicate a positive effect on the predicted results, negative values indicate a negative effect, and a more reddish color of the scatter indicates a larger value. In the figure, the TNT charge quantity has a positive effect on the size of the explosion crater, while the compressive strength and explosion distance have a negative effect. These are unidirectional effects, but the interaction of multiple factors under the effect is a very complex problem, so the subsequent interaction of multiple factors requires further study and analysis.

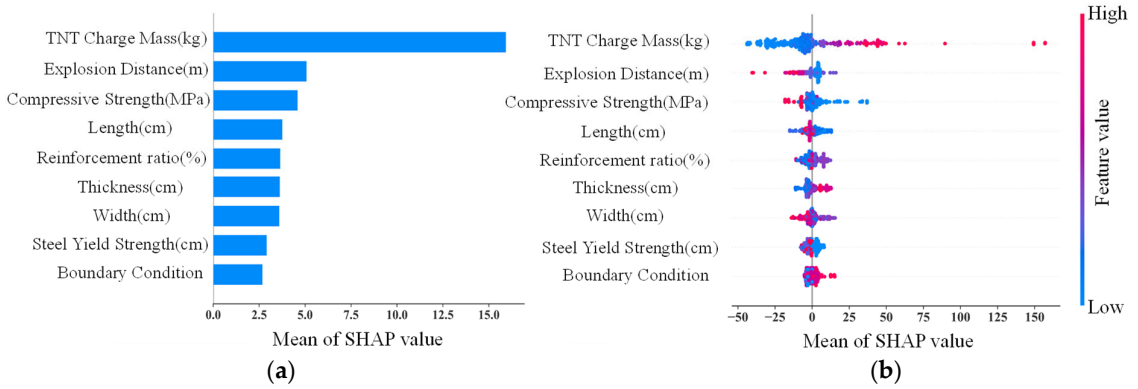


Figure 14. Feature importance analysis of XGBoost: (**a**) ranking the importance of impact factors; (**b**) crater size influence factor SHAP value.

According to the ranking of the importance of features, TNT charge mass, explosion distance, and compressive strength were selected as specific features for SHAP dependency analysis. In Figure 15a, when the TNT charge mass $\leq$ 2.5 kg, a change in explosion distance will not cause a large change in SHAP value, indicating that the explosion crater size is not sensitive to the change in explosion distance at this time. When the TNT charge mass > 2.5 kg, with the decrease in the explosion distance, the SHAP value increased significantly, so this time the explosion crater size is very sensitive to the explosion distance. In Figure 15b, when the compressive strength $\leq$ 50 MPa, both TNT charge mass and compressive strength have a significant influence on explosion crater size. When the compressive strength > 50 MPa, the influence of the TNT charge mass on the explosion crater size is still significant, but the slope of SHAP values corresponding to compressive strength at this time is relatively gentle, indicating that the compressive strength at this time has no significant influence on the explosion crater size. In summary, the results show that SHAP gives the detailed influence law and influence interval of different features on the explosion crater size of RC slabs, which provides a further reference for practical engineering.

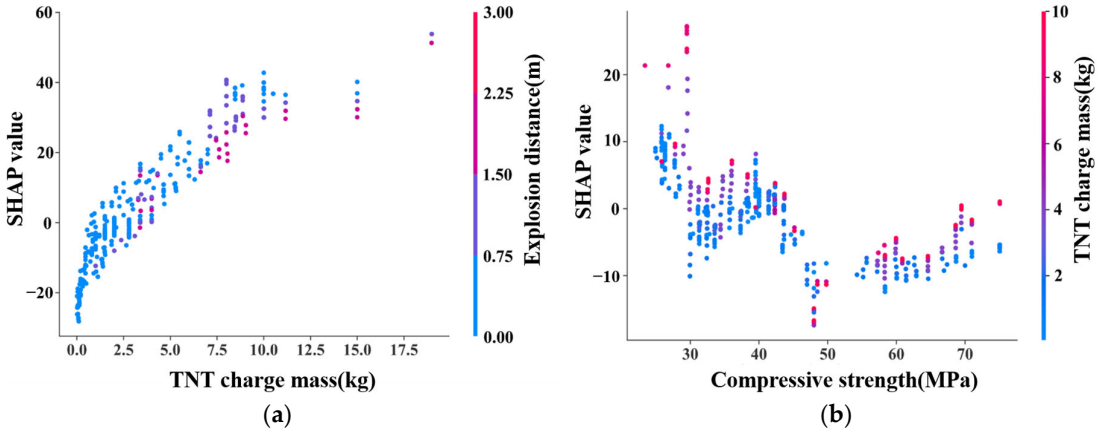


Figure 15. Feature dependency analysis: (**a**) TNT charge mass and explosion distance; (**b**) compressive strength and TNT charge mass.

5. Failure Mode Prediction Models

In this section, the damage modes of RC slabs under blast loading are predicted using the above six ML models with default parameters. Since the data collected from the literature lack the necessary failure modes, the failure modes are predicted in this section using 300 sets of data from supplementary simulations in Section 2.2, of which 125 sets are for BF, 95 sets are for BSF, and 80 sets are for SF.

In order to select the final prediction model, this section applies the method of probability confusion matrix [71] to perform an evaluation of the ML models (Figure 16). The method provides a visual representation of the prediction results for each failure mode, with the diagonal values indicating the probability of correct prediction for each failure mode. Comparing the six classification models, we can find that the CatBoost model has the best prediction performance and is the best choice for predicting the failure modes of the RC slabs, with the following results: 121 (97%) correctly predicted points in the BF mode, four (3%) incorrectly fell in the BSF, and no incorrect points in the SF; 80 (84%) correctly predicted points in the BSF mode, with five (5%) and 10 (11%) prediction points falling incorrectly under BF and SF, respectively; 74 (93%) correct prediction points under SF mode and one (1%) and five (6%) points falling incorrectly under BF and BSF, respectively.

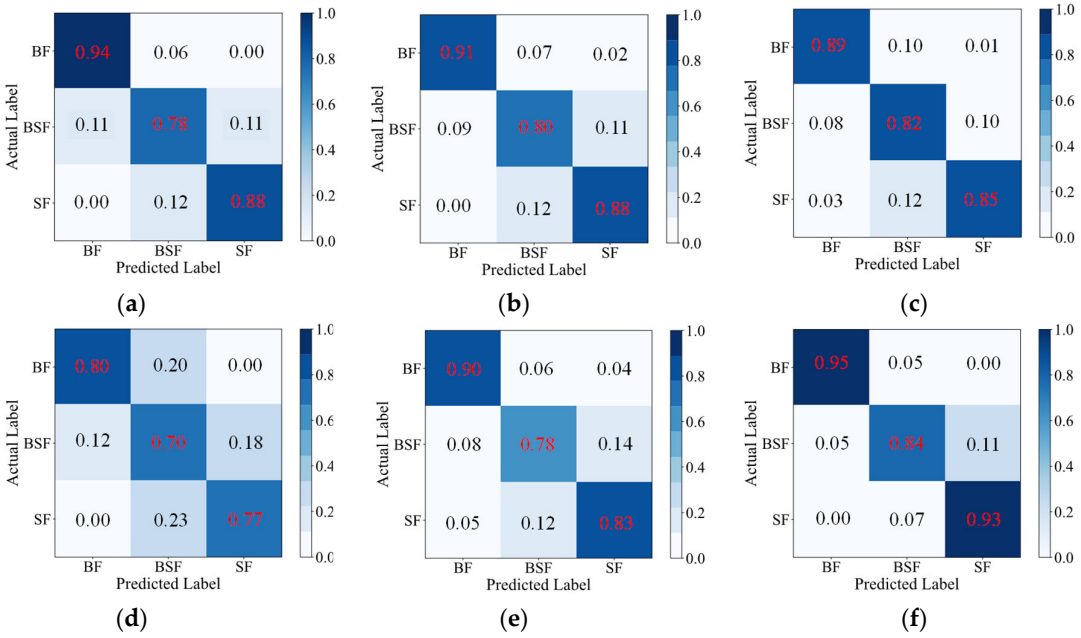


Figure 16. Probabilistic confusion matrices for multiple algorithms: (**a**) XGBoost; (**b**) BPNN; (**c**) SVC; (**d**) RF; (**e**) LightGBM; (**f**) CatBoost.

In order to have a comprehensive evaluation of classification tasks, this section introduces four evaluation indicators of classification tasks: Accuracy, Precision, Recall, and Fl-score. Their formulas are shown in Equations (10)–(13). Precision is used to measure the accuracy of the model to predict positive types; Recall is used to measure the ability of the model to find all positive types of samples; F1-score is the harmonic average of accuracy rate and recall rate, and synthesizes the performance of both; Accuracy is used to measure the overall prediction ability of the model.

$$Precision = \frac{TP}{TP + FP} \tag{10}$$

$$Recall = \frac{TP}{TP + FN} \tag{11}$$

$$F1 - score = \frac{2 \times Precision \times Recall}{Precision + Recall} \tag{12}$$

$$Accuracy = \frac{TP + TN}{TP + FP + TN + FN} \tag{13}$$

where TP (True Positive) and TN (True Negative) represent the number of samples that are correctly predicted as positive and negative classes, respectively. FP (False Positive)

denotes samples that are actually negative but incorrectly predicted as positive by the model, while FN (False Negative) refers to samples that are actually positive but incorrectly predicted as negative.

Table 11 gives the evaluation metrics of different ML models for predicting the failure modes of RC slabs after 10-CV. The CatBoost model has the highest prediction accuracy of 0.91, with F1-score of 0.95, 0.86, and 0.91 for its BF, BSF, and SF modes, followed closely by the XGBoost and BPNN models, which have a prediction accuracy of 0.87 and 0.86, while the RF model has the worst prediction, with a prediction accuracy of a tight 0.76. By comparing the above different algorithms for predicting failure modes, it can also be seen that the results for the two modes BF and SF are better than the BSF mode, and this difference may be due to the fact that the BSF mode is more complex. Comparing the different algorithms in Figure 16 and Table 11, it can be concluded that CatBoost has the best prediction performance for the failure mode of RC slabs. Therefore, the CatBoost model is chosen as the prediction model for the failure mode of RC slabs under blast loading. The establishment of this model provides a scientific basis for the evaluation of antiknock performance and structural design optimization of RC slab under blast loading, which is helpful to take more comprehensive load conditions and failure mechanisms into account in the design and production of structures, and improve the overall antiknock performance of structures.

Table 11. Performance index evaluation.

ML Model	Failure Mode	Precision	Recall	F1-Score	Accuracy
XGBoost	BF	0.90	0.94	0.92	0.87
	BSF	0.81	0.78	0.79	
	SF	0.89	0.88	0.88	
BPNN	BF	0.91	0.91	0.91	0.86
	BSF	0.81	0.80	0.80	
	SF	0.87	0.88	0.87	
SVC	BF	0.89	0.89	0.89	0.85
	BSF	0.79	0.82	0.80	
	SF	0.89	0.85	0.87	
RF	BF	0.87	0.80	0.83	0.76
	BSF	0.62	0.70	0.66	
	SF	0.81	0.77	0.79	
LightGBM	BF	0.87	0.90	0.88	0.84
	BSF	0.81	0.78	0.79	
	SF	0.82	0.83	0.82	
CatBoost	BF	0.95	0.95	0.95	0.91
	BSF	0.88	0.84	0.86	
	SF	0.89	0.93	0.91	

6. Conclusions

In this study, six ML models were trained using data obtained from the open literature and supplementary numerical simulations, and the optimal two ML models were obtained by comparing the structural damage prediction models in terms of metrics evaluation, data point distribution, and model response residuals, and the failure mode prediction models in terms of metrics evaluation and confusion matrix. On this basis, based on the SHAP algorithm, significance and correlation analyses of the features were carried out, and the results obtained can provide guidance for the blast-resistant design of RC slabs. The main conclusions of this paper are as follows:

1. Among the six structural damage prediction models, the XGBoost model has the best prediction effect on crater size. Its fitting values R^2 and EVS on the test set are 0.979 and 0.981, respectively. The error index MSE is 0.675, MAE is 0.379, MAPE is 3.639, and MSLE is 0.020. In contrast, the SVR model has the worst prediction effect;
2. Using on the SHAP algorithm to rank the importance of the features affecting the size of the explosion crater and dependence analysis, the results show that the TNT charge mass, explosion distance, and compressive strength have the greatest impact on the size of the explosion crater, and the interaction of each two features has an interval variation rule on the impact of the crater size;
3. In the comparison of the six failure mode ML algorithms, the CatBoost model has the highest prediction accuracy with an overall accuracy of 91%, where the accuracy of predicting BF, BSF, and SF is 95%, 84%, and 93%, respectively. The results show that the CatBoost model can accurately predict the failure modes of RC slabs under blast loading.

Author Contributions: Conceptualization, J.Y.; Methodology, Y.H.; Software, J.Y. and Y.H.; Validation, D.P.; Formal analysis, D.P.; Investigation, D.P.; Resources, J.S.; Data curation, J.S. and Y.Z.; Writing—original draft, Y.H.; Writing—review & editing, J.S.; Visualization, J.Y.; Supervision, J.S. and Y.Z.; Project administration, Y.Z. All authors have read and agreed to the published version of the manuscript.

Funding: This research received no external funding.

Data Availability Statement: The data presented in this study are available on request from the corresponding author.

Conflicts of Interest: Author Dang Peng was employed by Beijing Tianhe Qianyuan New Material Co., Ltd. The remaining authors declare that the research was conducted in the absence of any commercial or financial relationships that could be construed as a potential conflict of interest.

References

1. Zhao, C.; Chen, J. Damage mechanism and mode of square reinforced concrete slab subjected to blast loading. *Theor. Appl. Fract. Mech.* **2013**, *63*, 54–62. [CrossRef]
2. Zhao, C.; Chen, J.; Wang, Y.; Lu, S. Damage mechanism and response of reinforced concrete containment structure under internal blast loading. *Theor. Appl. Fract. Mech.* **2012**, *61*, 12–20. [CrossRef]
3. Zhao, C.; Lu, X.; Wang, Q.; Gautam, A.; Wang, J.; Mo, Y. Experimental and numerical investigation of steel-concrete (SC) slabs under contact blast loading. *Eng. Struct.* **2019**, *196*, 109337. [CrossRef]
4. Zhao, C.; Wang, Q.; Lu, X.; Huang, X.; Mo, Y. Blast resistance of small-scale RCS in experimental test and numerical analysis. *Eng. Struct.* **2019**, *199*, 109610. [CrossRef]
5. Army, U. Fundamentals of protective design for conventional weapons. In *Technical Manual*; TM 5-855-1; Department of the Army: The Pentagon, WV, USA, 1986.
6. U.S. Department of Defense. *Structures to Resist the Effects of Accidental Explosions*; UFC 3-340-02; U.S. Department of Defense: Arlington County, WV, USA, 2008.
7. Huang, X.; Bao, H.; Hao, Y.; Hao, H. Damage assessment of two-way RC slab subjected to blast load using mode approximation approach. *Int. J. Struct. Stab. Dyn.* **2017**, *17*, 1750013. [CrossRef]
8. Karmakar, S.; Shaw, A. Response of RC plates under blast loading using FEM-SPH coupled method. *Eng. Fail. Anal.* **2021**, *125*, 105409. [CrossRef]
9. Wu, J.; Zhou, Y.; Zhang, R.; Liu, C.; Zhang, Z. Numerical simulation of reinforced concrete slab subjected to blast loading and the structural damage assessment. *Eng. Fail. Anal.* **2020**, *118*, 104926. [CrossRef]
10. Zhao, X.; Wang, G.; Lu, W.; Yan, P.; Chen, M.; Zhou, C. Damage features of RC slabs subjected to air and underwater contact explosions. *Ocean Eng.* **2018**, *147*, 531–545. [CrossRef]
11. Zhou, X.; Kuznetsov, V.; Hao, H.; Waschl, J. Numerical prediction of concrete slab response to blast loading. *Int. J. Impact Eng.* **2008**, *35*, 1186–1200. [CrossRef]
12. Kumar, V.; Kartik, K.; Iqbal, M.A. Experimental and numerical investigation of reinforced concrete slabs under blast loading. *Eng. Struct.* **2020**, *206*, 110125. [CrossRef]

13. Morales-Alonso, G.; Cendón, D.A.; Gálvez, F.; Erice, B.; Sánchez-Gálvez, V. Blast response analysis of reinforced concrete slabs: Experimental procedure and numerical simulation. *J. Appl. Mech.* **2011**, *78*, 051010. [CrossRef]
14. Ning, J.; Yang, S.; Ma, T.; Xu, X. Fragment behavior of concrete slab subjected to blast loading. *Eng. Fail. Anal.* **2022**, *138*, 106370. [CrossRef]
15. Shi, Y.; Wang, J.; Cui, J. Experimental studies on fragments of reinforced concrete slabs under close-in explosions. *Int. J. Impact Eng.* **2020**, *144*, 103630. [CrossRef]
16. Wang, W.; Zhang, D.; Lu, F.; Wang, S.-C.; Tang, F. Experimental study and numerical simulation of the damage mode of a square reinforced concrete slab under close-in explosion. *Eng. Fail. Anal.* **2013**, *27*, 41–51. [CrossRef]
17. Wu, C.; Nurwidayati, R.; Oehlers, D.J. Fragmentation from spallation of RC slabs due to airblast loads. *Int. J. Impact Eng.* **2009**, *36*, 1371–1376. [CrossRef]
18. Chiquito, M.; López, L.M.; Castedo, R.; Santos, A.P.; Pérez-Caldentey, A. Full-Scale Field Tests on Concrete Slabs Subjected to Close-In Blast Loads. *Buildings* **2023**, *13*, 15. [CrossRef]
19. İskenderoğlu, F.C.; Baltacioğlu, M.K.; Demir, M.H.; Baldinelli, A.; Barelli, L.; Bidini, G. Comparison of support vector regression and random forest algorithms for estimating the SOFC output voltage by considering hydrogen flow rates. *Int. J. Hydrogen Energy* **2020**, *45*, 35023–35038. [CrossRef]
20. Mohri, M.; Rostamizadeh, A.; Talwalkar, A. *Foundations of Machine Learning*; MIT Press: Cambridge, MA, USA, 2018.
21. Neapolitan, R.E.; Jiang, X. *Artificial Intelligence: With an Introduction to Machine Learning*; CRC Press: Boca Raton, FL, USA, 2018.
22. Park, B.H.; Chae, C.K. Development of correlation equations on hydrogen properties for hydrogen refueling process by machine learning approach. *Int. J. Hydrogen Energy* **2022**, *47*, 4185–4195. [CrossRef]
23. Zhao, C.; Zhu, Y.; Zhou, Z. Machine learning-based approaches for predicting the dynamic response of RC slabs under blast loads. *Eng. Struct.* **2022**, *273*, 115104. [CrossRef]
24. Li, Z.-X.; Zhang, X.; Shi, Y.; Wu, C.; Li, J. Predication of the residual axial load capacity of CFRP-strengthened RC column subjected to blast loading using artificial neural network. *Eng. Struct.* **2021**, *242*, 112519. [CrossRef]
25. Neto, L.B.; Saleh, M.; Pickerd, V.; Yiannakopoulos, G.; Mathys, Z.; Reid, W. Rapid mechanical evaluation of quadrangular steel plates subjected to localised blast loadings. *Int. J. Impact Eng.* **2020**, *137*, 103461. [CrossRef]
26. Dennis, A.A.; Pannell, J.J.; Smyl, D.J.; Rigby, S.E. Prediction of blast loading in an internal environment using artificial neural networks. *Int. J. Prot. Struct.* **2021**, *12*, 287–314. [CrossRef]
27. Almustafa, M.; Nehdi, M. Machine learning model for predicting structural response of RC slabs exposed to blast loading. *Eng. Struct.* **2020**, *221*, 111109. [CrossRef]
28. Xu, Y.; Huang, Y.; Ma, G. A beetle antennae search improved BP neural network model for predicting multi-factor-based gas explosion pressures. *J. Loss Prev. Process Ind.* **2020**, *65*, 104117. [CrossRef]
29. Hemmatian, B.; Casal, J.; Planas, E.; Hemmatian, B.; Rashtchian, D. Prediction of BLEVE mechanical energy by implementation of artificial neural network. *J. Loss Prev. Process Ind.* **2020**, *63*, 104021. [CrossRef]
30. Pannell, J.J.; Panoutsos, G.; Cooke, S.B.; Pope, D.J.; Rigby, S.E. Predicting specific impulse distributions for spherical explosives in the extreme near-field using a Gaussian function. *Int. J. Prot. Struct.* **2021**, *12*, 437–459. [CrossRef]
31. Li, Q.; Wang, Y.; Li, L.; Hao, H.; Wang, R.; Li, J. Prediction of BLEVE loads on structures using machine learning and CFD. *Process Saf. Environ. Prot.* **2023**, *171*, 914–925. [CrossRef]
32. Cai, R.; Li, Y.; Zhang, C.; Cao, H.; Qi, H.; Mao, J. Size effect on reinforced concrete slabs under direct contact explosion. *Eng. Struct.* **2022**, *252*, 113656. [CrossRef]
33. Castedo, R.; Segarra, P.; Alañon, A.; Lopez, L.; Santos, A.; Sanchidrian, J. Air blast resistance of full-scale slabs with different compositions: Numerical modeling and field validation. *Int. J. Impact Eng.* **2015**, *86*, 145–156. [CrossRef]
34. He, F. Static Limit Analysis and Nonlinear Explosion Response of Reinforced Concrete Slabs. Master's Thesis, South China University of Technology, Guangzhou, China, 2018.
35. Hou, X.; Lu, H.; Chen, W.; Zhou, B.; Wei, X. Numerical simulation of blast-resistances for high strength RC slabs under non-contact explosion loading. *Prot. Eng.* **2016**, *38*, 34–43. (In Chinese)
36. Hou, X.W.; Lu, H.B.; Chen, W.X.; Zhou, B.K.; Liu, Y. Analysis on the Anti-contact Explosion Failure Patterns of High Strength RC Slabs. *J. Wuhan Univ. Technol.* **2013**, *35*, 96–100. (In Chinese)
37. Jiachao, S.; Xiaowei, C.; Yongjun, D.; Yong, Y. Dynamic response of mesoscopic plain/reinforced concrete slabs under blast loading. *Explos. Shock Waves* **2019**, *39*, 113101-1–113101-11. (In Chinese)
38. Li, J.; Wu, C.; Hao, H. Investigation of ultra-high performance concrete slab and normal strength concrete slab under contact explosion. *Eng. Struct.* **2015**, *102*, 395–408. [CrossRef]
39. Li, J.; Wu, C.; Hao, H.; Wang, Z.; Su, Y. Experimental investigation of ultra-high performance concrete slabs under contact explosions. *Int. J. Impact Eng.* **2016**, *93*, 62–75. [CrossRef]
40. Liu, Z.; Zhao, X.; Fang, H.; Wang, G.; Shi, M. Investigation on the damage features and dynamic response of reinforced concrete slabs with polyurethane sacrificial cladding under close-range explosions. *Constr. Build. Mater.* **2023**, *395*, 132149. [CrossRef]

41. Qiang, W. Study on Dynamic Response of Reinforced Concrete Slab and Containment Dome with 60° Configuration under Blast Load. Master's Thesis, Hefei University of Technology, Hefei, China, 2019.
42. Ruggiero, A.; Bonora, N.; Curiale, G.; De Muro, S.; Iannitti, G.; Marfia, S.; Sacco, E.; Scafati, S.; Testa, G. Full scale experimental tests and numerical model validation of reinforced concrete slab subjected to direct contact explosion. *Int. J. Impact Eng.* **2019**, *132*, 103309. [CrossRef]
43. Shi, Y.; Chen, L.; Wang, Z.; Zhang, X. Field tests on spalling damage of reinforced concrete slabs under close-in explosions. *Int. J. Prot. Struct.* **2015**, *6*, 389–401. [CrossRef]
44. Xu, S.L.; Li, R.; Li, Q.H.; Chen, B.K. Numerical simulation of functionally graded slabs of ultra-high toughness cementitious composites under contact explosion. *Eng. Mech.* **2020**, *37*, 123–133, 178. (In Chinese)
45. Wang, W.; Huo, Q.; Yang, J.-C.; Wang, J.-H.; Wang, X. Experimental investigation of ultra-early-strength cement-based self-compacting high strength concrete slabs (URCS) under contact explosions. *Def. Technol.* **2023**, *24*, 326–339. [CrossRef]
46. Wang, W.; Zhang, D.; Lu, F.; Wang, S.-C.; Tang, F. Experimental study on scaling the explosion resistance of a one-way square reinforced concrete slab under a close-in blast loading. *Int. J. Impact Eng.* **2012**, *49*, 158–164. [CrossRef]
47. Wei, W. Study on Damage Effects and Assessments Method of Reinforced Concrete Structural Members under Blast loading. Ph.D. Thesis, National University of Defense Technology, Changsha, China, 2012.
48. Xu, W. Damage Evolution Process and Dynamic Response Analysis of Reinforced Concrete Slabs under Blast Loading. Master's Thesis, Zhengzhou University, Zhengzhou China, 2022.
49. Yao, J.; Li, S.; Zhang, P.; Deng, S.; Zhou, G. Dynamic Response and Damage Characteristics of Large Reinforced Concrete Slabs under Explosion. *Appl. Sci.* **2023**, *13*, 12552. [CrossRef]
50. Zhao, X.; Wang, G.; Lu, W.; Yang, G.; Chen, M.; Yan, P. Experimental investigation of RC slabs under air and underwater contact explosions. *Eur. J. Environ. Civ. Eng.* **2021**, *25*, 190–204. [CrossRef]
51. Rhouma, M.B.; Maazoun, A.; Aminou, A.; Belkassem, B.; Tysmans, T.; Lecompte, D. Damage Assessment of Laboratory-Scale Reinforced Concrete Columns Under Localized Blast Loading. *Buildings* **2025**, *15*, 1003. [CrossRef]
52. Mikolov, T.; Chen, K.; Corrado, G.; Dean, J. Efficient estimation of word representations in vector space. *arXiv* **2013**, arXiv:1301.3781.
53. Bengio, Y.; Ducharme, R.; Vincent, P.; Jauvin, C. A neural probabilistic language model. *J. Mach. Learn. Res.* **2003**, *3*, 1137–1155.
54. Topuz, B.; Alp, N.Ç. Machine learning in architecture. *Autom. Constr.* **2023**, *154*, 105012. [CrossRef]
55. Chen, T.; Guestrin, C. Xgboost: A scalable tree boosting system. In Proceedings of the 22nd ACM Sigkdd International Conference on Knowledge Discovery and Data Mining, San Francisco, CA, USA, 13–17 August 2016; pp. 785–794.
56. Friedman, J.H. Greedy function approximation: A gradient boosting machine. *Ann. Stat.* **2001**, *29*, 1189–1232. [CrossRef]
57. Dong, J.; Chen, Y.; Yao, B.; Zhang, X.; Zeng, N. A neural network boosting regression model based on XGBoost. *Appl. Soft Comput.* **2022**, *125*, 109067. [CrossRef]
58. Song, K.; Yan, F.; Ding, T.; Gao, L.; Lu, S. A steel property optimization model based on the XGBoost algorithm and improved PSO. *Comput. Mater. Sci.* **2020**, *174*, 109472. [CrossRef]
59. Wang, L.; Zeng, Y.; Chen, T. Back propagation neural network with adaptive differential evolution algorithm for time series forecasting. *Expert Syst. Appl.* **2015**, *42*, 855–863. [CrossRef]
60. Sarothi, S.Z.; Ahmed, K.S.; Khan, N.I.; Ahmed, A.; Nehdi, M.L. Predicting bearing capacity of double shear bolted connections using machine learning. *Eng. Struct.* **2022**, *251*, 113497. [CrossRef]
61. Vapnik, V.N. *The Nature of Statistical Learning Theory*; Wiley: Hoboken, NJ, USA, 1995.
62. Farnaaz, N.; Jabbar, M. Random forest modeling for network intrusion detection system. *Procedia Comput. Sci.* **2016**, *89*, 213–217. [CrossRef]
63. Ke, G.; Meng, Q.; Finley, T.; Wang, T.; Chen, W.; Ma, W.; Ye, Q.; Liu, T.-Y. Lightgbm: A highly efficient gradient boosting decision tree. In *Advances in Neural Information Processing Systems 30 (NIPS 2017), Proceedings of the 31st Conference on Neural Information Processing Systems (NIPS 2017), Long Beach, CA, USA, 2017*; NeurIPS: San Diego, CA, USA, 2017; Volume 30, pp. 3146–3154.
64. Hancock, J.T.; Khoshgoftaar, T.M. CatBoost for big data: An interdisciplinary review. *J. Big Data* **2020**, *7*, 94. [CrossRef] [PubMed]
65. Ye, M.; Li, L.; Yoo, D.-Y.; Li, H.; Zhou, C.; Shao, X. Prediction of shear strength in UHPC beams using machine learning-based models and SHAP interpretation. *Constr. Build. Mater.* **2023**, *408*, 133752. [CrossRef]
66. Lazaridis, P.C.; Kavvadias, I.E.; Demertzis, K.; Iliadis, L.; Papaleonidas, A.; Vasiliadis, L.K.; Elenas, A. Structural damage prediction under seismic sequence using neural networks. In Proceedings of the 8th International Conference on Computational Methods in Structural Dynamics and Earthquake Engineering (ECCOMAS-COMPDYN 2021), Athens, Greece, 28–30 June 2021.
67. Duran, B.; Eftekhar Azam, S.; Sanayei, M. Leveraging Deep Learning for Robust Structural Damage Detection and Classification: A Transfer Learning Approach via CNN. *Infrastructures* **2024**, *9*, 229. [CrossRef]
68. Reifarth, C.; Castedo, R.; Santos, A.; Chiquito, M.; López, L.; Pérez-Caldentey, A.; Martínez-Almajano, S.; Alañon, A. Numerical and experimental study of externally reinforced RC slabs using FRPs subjected to close-in blast loads. *Int. J. Impact Eng.* **2021**, *156*, 103939. [CrossRef]

69. Zhou, T.; Yang, J.; Zhan, X.; Pei, Y.; Zhang, J.; Chen, H.; Zhu, F. Data-driven method and interpretability analysis for transient voltage stability assessment. *Power Syst. Technol.* **2021**, *45*, 4416–4425.
70. Lundberg, S.M.; Lee, S.-I. A unified approach to interpreting model predictions. In *Advances in Neural Information Processing Systems 30 (NIPS 2017), Proceedings of the 31st Conference on Neural Information Processing Systems (NIPS 2017), Long Beach, CA, USA, 2017*; NeurIPS: San Diego, CA, USA, 2017; Volume 30, pp. 4765–4774.
71. Nguyen, K.T.; Medjaher, K. A new dynamic predictive maintenance framework using deep learning for failure prognostics. *Reliab. Eng. Syst. Saf.* **2019**, *188*, 251–262. [CrossRef]

Disclaimer/Publisher's Note: The statements, opinions and data contained in all publications are solely those of the individual author(s) and contributor(s) and not of MDPI and/or the editor(s). MDPI and/or the editor(s) disclaim responsibility for any injury to people or property resulting from any ideas, methods, instructions or products referred to in the content.